

# Supplementary Materials for Magnetochiral Tunneling in Paramagnetic $\text{Co}_{1/3}\text{NbS}_2$

Seongjoon Lim<sup>†</sup>, Sobhit Singh<sup>†</sup>, Fei-Ting Huang, Shangke Pan, Kefeng Wang, Jaewook Kim,  
Jinwoong Kim, David Vanderbilt<sup>\*</sup>, Sang-Wook Cheong<sup>\*</sup>

<sup>†</sup>These authors contributed equally to this work.

<sup>\*</sup>Correspondence to: [dhv@physics.rutgers.edu](mailto:dhv@physics.rutgers.edu), [sangc@physics.rutgers.edu](mailto:sangc@physics.rutgers.edu)

**This PDF file includes:**

Supplementary Note 1 to 11  
Figs. S1 to S13  
Tables S1 and S2

## Supplementary Text

### Supplementary Note 1.

#### Symmetry Operational Similarity Consideration

The concept of symmetry operational similarity (SOS) involves the examination of broken symmetries present in the constituents of various physical phenomena (1–3). The experimental components of a measurement, including a subject material, a measuring probe, any external stimuli, and a measured/induced property, are referred to as constituents. We compare the broken symmetries of a subject material combined with a measuring probe and any external stimuli, which we refer as specimen constituents, with the broken symmetries of a measured or induced property. To set up a meaningful physical measurement, it is necessary to demonstrate an SOS relationship (2) between the specimen constituent and the measured property, meaning that the specimen constituent has the same or more broken symmetries than the measured property. In other words, if a specimen constituent is invariant under a symmetry operation, the measured quantity cannot have any property that is not invariant under the symmetry, which is a rephrasing of the Neumann’s principle with inclusion of more experimental components (1). The SOS approach has been successful in uncovering the symmetry structures present in various seemingly unrelated physical phenomena and has even predicted novel and intriguing measurement setups (1, 4) and the current result is one of such examples. In this note, we further examine the specific broken structural symmetries that can associate with an induction of a magnetic signal through a dynamic coupling with a measuring probe carrying a linear momentum, and we reveal all candidate structures in terms of crystallographic point group.

Fig. S1 schematically shows a linear momentum ( $\mathbf{k}$ ) carried by a measuring probe and a magnetization ( $\mathbf{M}$ ) induced by a dynamic coupling between  $\mathbf{k}$  and a broken structural symmetry of a material being measured. The measurement of such a coupling detects a magnetic signal that originates from the contrast between two magnetizations “ $+\mathbf{M}$ ” and “ $-\mathbf{M}$ ”. It is similar to an optical circular dichroism, which measures the difference between left-handed and right-handed light. We say that such a coupling is present if and only if there is no symmetry connecting the two situations in which  $\mathbf{M}$  is changed without altering  $\mathbf{k}$ . (This is the same as saying that there are no invariants in the energy that are first order in the relevant component of  $\mathbf{M}$ , regardless of the order in  $\mathbf{k}$ .) Fig. S1A depicts this situation for the case of a parallel arrangement of  $\mathbf{M}$  and  $\mathbf{k}$  ( $\mathbf{M}//\mathbf{k}$  coupling). In the absence of a subject material, symmetries such as  $i\otimes T$  (spatial inversion followed by time reversal),  $m_z\otimes T$  ( $m_z$  mirror followed by time reversal), and simple  $m_x$  and  $m_y$  mirrors do reverse  $\mathbf{M}$  in this way. Thus, to ensure that there is no symmetry operation connecting the reversal of  $\mathbf{M}$ , the symmetries  $\{i\otimes T, m_x, m_y, m_z\otimes T\}$  should be broken by the structure of a subject material. We refer the point groups that satisfy this requirement as being “*active*” in the  $\mathbf{M}//\mathbf{k}$  coupling.

For the  $\mathbf{M}//\mathbf{k}$  case, we need to take into account that the experimental geometry allows free rotation around the  $z$  axis. As a result, we can drop  $m_z\otimes T$  from the list, as it results from the composition of  $C_{2z}$  with  $i\otimes T$ . This results in the shorter list shown in Fig. S1A. Importantly, note that  $T$  itself does not have to be broken to permit  $\mathbf{M}//\mathbf{k}$  activity, since  $T$  reverses  $\mathbf{k}$  as well as  $\mathbf{M}$ . When we consider time-reversal invariant materials, a symmetry  $X$  is present if and only if  $X\otimes T$  is present, so that we can replace  $i\otimes T$  by  $i$  in the list of needed broken symmetries. Thus, our list of spatial symmetries that need to be broken for active  $\mathbf{M}//\mathbf{k}$  coupling in a nonmagnetic material can be reduced to just  $\{i, m_x, m_y\}$ .

In a similar manner, we analyze  $\mathbf{M} \perp \mathbf{k}$  coupling as depicted in Fig. S1B. In this case there is no free rotation. The symmetry operations that reverse  $\mathbf{M}$  but not  $\mathbf{k}$  are  $\{i \otimes T, m_y, C_{2z}, C_{3z}, C_{2x} \otimes T\}$ , as shown in Fig. S1B. As a result, for time-reversal invariant materials, symmetries  $\{i, m_y, C_{2z}, C_{3z}, C_{2x}\}$  are required to be broken to activate  $\mathbf{M} \perp \mathbf{k}$  coupling.

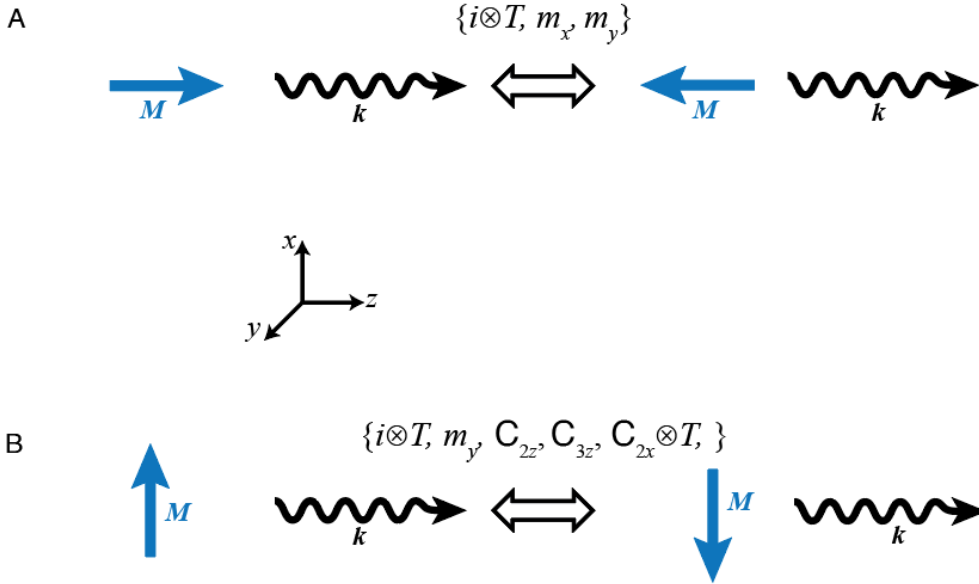


**Fig. S1. Symmetry Operations that Reverse the Induced Magnetization in a Magnetic Probe (A)  $\mathbf{M} // \mathbf{k}$  coupling:** When a momentum ( $\mathbf{k}$ ) and an induced magnetization ( $\mathbf{M}$ ) are parallel to each other, applying combined time-reversal ( $T$ ) and spatial inversion ( $i$ ) or mirror symmetry operation parallel to  $\mathbf{k}$  (e.g.  $m_x$  or  $m_y$ ) flips the direction of  $\mathbf{M}$ . This means that only a material that breaks these symmetries can dynamically couple to the probe and produce  $\mathbf{M}$ . If a material has one of the listed symmetries, then the unbroken symmetry ensures that two measurements with opposite  $\mathbf{M}$  are equivalent, which suppresses the magnetic signal. **(B)  $\mathbf{M} \perp \mathbf{k}$  coupling:** When  $\mathbf{k}$  and  $\mathbf{M}$  are perpendicular to each other,  $\{i \otimes T, m_y, C_{2z}, C_{3z}, C_{2x} \otimes T\}$  are the symmetries that connect the reversal of  $\mathbf{M}$ . Any material that breaks these symmetry operations can produce an induced  $\mathbf{M}$  that is perpendicular to  $\mathbf{k}$ . For time-reversal invariant non-magnetic materials, broken  $\{i, m_x, m_y\}$  are required for  $\mathbf{M} // \mathbf{k}$  coupling, and broken  $\{i, m_y, C_{2z}, C_{3z}, C_{2x}\}$  are required for  $\mathbf{M} \perp \mathbf{k}$  coupling.

To figure out the potential set of crystallographic point groups that can be active in  $\mathbf{M} // \mathbf{k}$  coupling, first, we list all the symmetry operations of the 21 noncentrosymmetric point groups in Table S1. For simplicity, we excluded the centrosymmetric point groups that inherently suppress  $\mathbf{M} // \mathbf{k}$  and  $\mathbf{M} \perp \mathbf{k}$  couplings due to their inversion symmetry  $i$ . We shaded rows with a point group that can be active in  $\mathbf{M} // \mathbf{k}$  coupling with blue color. Notably, all chiral point groups are included (1) as they lack mirror symmetry operation, so they are active to this type of coupling regardless of their orientation. Other non-chiral point groups can exhibit  $\mathbf{M} // \mathbf{k}$  coupling in a certain orientation. For those, we considered only high symmetry directions, by which we mean the directions related to the symmetries present in the point group being considered in addition to  $x$ ,  $y$ , and  $z$  directions. (for trigonal systems,  $[100]$  and  $[010]$  directions are included) For example, in the case of  $\bar{4}2m$ , which possesses symmetry operations,  $C_{2z}$   $S_{4z}$   $C_{2x}$   $C_{2y}$   $m_{[110]}$   $m_{[1-10]}$ , we considered  $\mathbf{k}$  propagating along  $x$ ,  $y$ ,  $z$ ,  $[110]$ , and  $[1-10]$ . As a result, two more point groups are included, as they can be active in  $\mathbf{M} // \mathbf{k}$  coupling when these vectors are oriented along a high-symmetry direction such as one of the rotational symmetry axes. Although the rest of the noncentrosymmetric point groups can still show  $\mathbf{M} // \mathbf{k}$  coupling for  $\mathbf{k}$  propagating along a lower-symmetry direction, we expect it to be subtle due to the suppression of the effect along the high symmetry directions. They are left without shading, being marked with mirror symmetries preventing them from meeting the requirement.

Table S2 shows the analysis that is relevant to  $\mathbf{M} \perp \mathbf{k}$  coupling, where the required broken spatial symmetries are  $\{i, m_y, C_{2z}, C_{3z}, C_{2x}\}$ . The two rotational symmetries  $\{C_{2z}, C_{2x}\}$  must be broken, permitting only the remaining  $C_{2y}$  symmetry to be present. The requirement can be met naturally by all the polar point groups by aligning their polar axis along the  $y$  direction, as they retain rotational symmetries along only one axis without a mirror symmetry to that axis (1). As a result, all polar point groups are active in  $\mathbf{M} \perp \mathbf{k}$  coupling, and are shaded in blue in the table. A few more point groups are also included after carefully examining the possible orientations of  $\mathbf{M}$  and  $\mathbf{k}$  along high symmetry directions. For all the other point groups, the rotational symmetries that mainly prevent them from meeting the requirement are highlighted in orange. Again, other point groups can still show  $\mathbf{M} \perp \mathbf{k}$  coupling for a  $\mathbf{k}$  direction along a low symmetric direction, but the effect will be subtle due to the suppression along the high symmetry directions.

Point Groups		Symmetry Operations	Note
<b>1</b>	$C_1$		Chiral
<b>2</b>	$C_2$	$C_{2y}$	Chiral
<b>"m"</b>	$C_{1h}$	$m_y$	
<b>222</b>	$D_2$	$C_{2z} C_{2x} C_{2y}$	Chiral
<b>"mm" 2</b>	$C_{2v}$	$C_{2z} m_x m_y$	
<b>4</b>	$C_4$	$C_{2z} C_{4z}$	Chiral
<b>4<math>\bar{2}</math></b>	$S_4$	$C_{2z} S_{4z}$	
<b>422</b>	$D_4$	$C_{2z} C_{4z} C_{2x} C_{2y} C_{2[110]} C_{2[1-10]}$	Chiral
<b>4"mm"</b>	$C_{4v}$	$C_{2z} C_{4z} m_x m_y m_{[110]} m_{[1-10]}$	
<b>4<math>\bar{2}</math>"m"</b>	$D_{2d}$	$C_{2z} S_{4z} C_{2x} C_{2y} m_{[110]} m_{[1-10]}$	
<b>3</b>	$C_3$	$C_{3z}$	Chiral
<b>32</b>	$D_3$	$C_{3z} C_{2[1-10]} C_{2[120]} C_{2[210]}$	Chiral
<b>3"m"</b>	$C_{3v}$	$C_{3z} m_{[100]} m_{[010]} m_{[110]}$	
<b>6</b>	$C_6$	$C_{2z} C_{3z} C_{6z}$	Chiral
<b>6<math>\bar{6}</math></b>	$C_{3h}$	$C_{3z} S_{6z} m_z$	
<b>622</b>	$D_6$	$C_{2z} C_{3z} C_{6z} C_{2[100]} C_{2[010]} C_{2[110]} C_{2[1-10]} C_{2[120]} C_{2[210]}$	Chiral
<b>6"mm"</b>	$C_{6v}$	$C_{2z} C_{3z} C_{6z} m_{[100]} m_{[010]} m_{[110]} m_{[1-10]} m_{[120]} m_{[210]}$	
<b>6m2</b>	$D_{3h}$	$C_{3z} S_{6z} C_{2[1-10]} C_{2[120]} C_{2[210]} m_z m_{[100]} m_{[010]} m_{[110]}$	
<b>23</b>	$T$	$C_{2z} C_{2x} C_{2y} C_{3[111]} C_{3[-11-1]} C_{3[1-1-1]} C_{3[-1-11]}$	Chiral
<b>432</b>	$O$	$C_{2z} C_{4z} C_{2x} C_{4x} C_{2y} C_{4y} C_{2[110]} C_{2[1-10]} C_{2[011]} C_{2[101]} C_{2[-101]} C_{2[01-1]}$	Chiral
<b>4<math>\bar{3}</math>"m"</b>	$T_d$	$C_{2z} S_{4z} C_{2x} S_{4x} C_{2y} S_{4y} C_{3[111]} C_{3[-11-1]} C_{3[1-1-1]} C_{3[-1-11]}$ $m_{[110]} m_{[011]} m_{[101]} m_{[1-10]} m_{[01-1]} m_{[-101]}$	

**Table S1. Crystallographic Point Groups Active in  $M//k$  Coupling.** The requirement is broken  $\{i, m_x, m_y\}$  for a time-reversal invariant structure. The symmetry operations that mainly prevent the requirement from being met are highlighted in orange, which are related to broken mirrors,  $\{m_x, m_y\}$ , and the consideration of freely allowed rotation around the  $z$  axis. As a result, point groups without any highlights, which can be active in  $M//k$  coupling, are shaded in blue color and are characterized by being chiral with a few more inclusions.

Point Groups	Symmetry Operations		Note
1	$C_1$		Polar
2	$C_2$	$C_{2y}$	Polar
"m"	$C_{1h}$	$m_y$	Polar
222	$D_2$	$C_{2z} C_{2x} C_{2y}$	
"mm" 2	$C_{2v}$	$C_{2z} m_x m_y$	Polar
4	$C_4$	$C_{2z} C_{4z}$	Polar
$\bar{4}$	$S_4$	$C_{2z} S_{4z}$	
422	$D_4$	$C_{2z} C_{4z} C_{2x} C_{2y} C_{2[110]} C_{2[1-10]}$	
4"mm"	$C_{4v}$	$C_{2z} C_{4z} m_x m_y m_{[110]} m_{[1-10]}$	Polar
4 $\bar{2}$ "m"	$D_{2d}$	$C_{2z} S_{4z} C_{2x} C_{2y} m_{[110]} m_{[1-10]}$	
3	$C_3$	$C_{3z}$	Polar
32	$D_3$	$C_{3z} C_{2[1-10]} C_{2[120]} C_{2[210]}$	
3"m"	$C_{3v}$	$C_{3z} m_{[100]} m_{[010]} m_{[110]}$	Polar
6	$C_6$	$C_{2z} C_{3z} C_{6z}$	Polar
$\bar{6}$	$C_{3h}$	$C_{3z} S_{6z} m_z$	
622	$D_6$	$C_{2z} C_{3z} C_{6z} C_{2[100]} C_{2[010]} C_{2[110]} C_{2[1-10]} C_{2[120]} C_{2[210]}$	
6"mm"	$C_{6v}$	$C_{2z} C_{3z} C_{6z} m_{[100]} m_{[010]} m_{[110]} m_{[1-10]} m_{[120]} m_{[210]}$	Polar
6 $\bar{m}2$	$D_{3h}$	$C_{3z} S_{6z} C_{2[1-10]} C_{2[120]} C_{2[210]} m_z m_{[100]} m_{[010]} m_{[110]}$	
23	T	$C_{2x} C_{2y} C_{2z} C_{3[111]} C_{3[-1-1]} C_{3[1-1-1]} C_{3[-1-11]}$	
432	O	$C_{2z} C_{4z} C_{2x} C_{4x} C_{2y} C_{4y} C_{2[110]} C_{2[1-10]} C_{2[011]} C_{2[101]} C_{2[01-1]} C_{2[-101]}$	
4 $\bar{3}$ "m"	$T_d$	$C_{2z} S_{4z} C_{2x} S_{4x} C_{2y} S_{4y} C_{3[111]} C_{3[-1-1]} C_{3[1-1-1]} C_{3[-1-11]}$ $m_{[110]} m_{[011]} m_{[101]} m_{[1-10]} m_{[01-1]} m_{[-101]}$	

**Table S2. Crystallographic Point Groups Active in  $M \perp k$  Coupling.** The requirement is broken  $\{i, m_y, C_{2z}, C_{3z}, C_{2x}\}$  for a time-reversal invariant structure. The symmetry operations that mainly prevent the requirement from being met are highlighted in orange. As a result, point groups without any highlight, which can be active in  $M \perp k$  coupling, are shaded rows with blue and are characterized by being polar with a few more inclusions.

In Fig. S2, we summarize the point groups that can be active in  $M//k$  and  $M \perp k$  couplings for  $k$  propagating along a high symmetry direction together with their various structural properties such as noncentrosymmetric, chiral, and polar structures. Point groups relevant to  $M//k$  coupling are shown in the red dashed box, while those relevant to  $M \perp k$  coupling are shown in the blue dashed box. The point group 622 ( $D_6$ ), to which  $\text{Co}_{1/3}\text{NbS}_2$  belongs, is also indicated. The result summarized here demonstrates that 20 out of 21 noncentrosymmetric point groups can potentially be active in current-induced magnetization with a proper arrangement of  $k$  and the orientation of a crystal. The summary presented in the diagram highlights the potential of using this prototype research technique to investigate the role of quantum geometric effects in a variety of non-magnetic material structures.

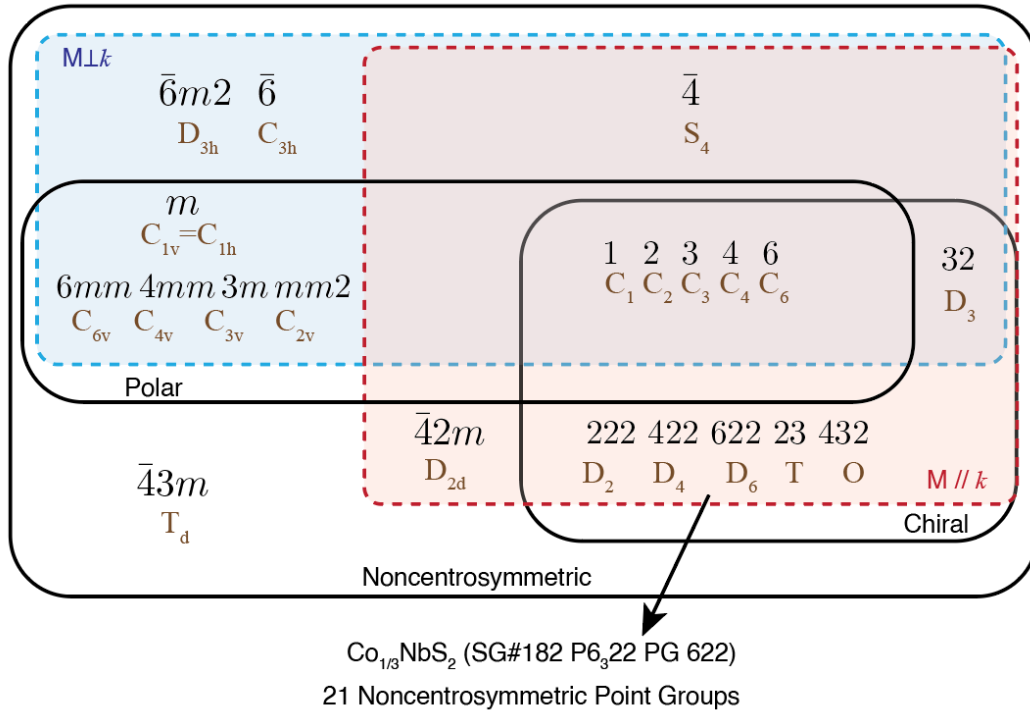


**Fig. S2. Diagram of Crystallographic Point Groups Relevant to  $M//k$  and  $M \perp k$  Couplings.** There are 21 noncentrosymmetric point groups that can be grouped based on their structural features such as chiral and polar structures. For  $M//k$  coupling, most cases are chiral point groups, which inherently lack any improper rotations such as inversion or mirror. For  $M \perp k$  coupling, the majority are polar point groups, which allow rotational symmetries along only one axis without accompanying mirror perpendicular to that axis. The structure of  $\text{Co}_{1/3}\text{NbS}_2$ , P6<sub>3</sub>22, belongs to the chiral point group 622 ( $D_6$ ) which is relevant to  $M//k$  coupling.

## Supplementary Note 2.

### Chiral Domain Observation using TEM

The existence of the topological vortex in the family of  $M_{1/3}(\text{Nb,Ta})\text{S}_2$  has been first reported in  $\text{Fe}_{1/3}\text{TaS}_2$  with  $\sqrt{3} \times \sqrt{3}$  superstructure as well as three types (A, B, and C) of antiphase domains (5) in the chiral space group,  $P6_322$ . We have been working on the growth of isostructural crystals and also on control of domain density, and the current report is the first one to show the topological vortex of  $\text{Co}_{1/3}\text{NbS}_2$ . So, in this note, we present our findings on formation of topological vortex and control of vortex density using cooling speed. Fig. S3A shows the diffraction pattern of  $\text{Co}_{1/3}\text{NbS}_2$  revealing the  $\sqrt{3} \times \sqrt{3}$  superstructure peaks in addition to the primitive  $1 \times 1$  peaks of  $\text{NbS}_2$  using selected area electron diffraction pattern. In the measurement, the crystals are furnace-cooled from the growth temperature. Figs. S3B and C depict the typical domain size formed by the furnace cooling together with the contrast reversal by selecting different diffraction conditions. We estimated the transition from the high temperature phase of  $P6_3/mmc$  to the low temperature chiral phase of  $P6_322$  to be around  $1000^\circ\text{C}$ . Figs. S3D and E are the diffraction pattern and real space domain observation of a quenched crystal from the temperature slightly above  $1000^\circ\text{C}$ . The dramatic increase of vortex density exhibits the possibility of Kibble-Zurek type disorder condensation mechanism (6) in the process of vortex formation.

### Temperature Dependence of Magnetic Susceptibility

In preparation for the STM/SP-STM measurement, we conducted a temperature-dependent measurement of the bulk magnetic susceptibility of a  $\text{Co}_{1/3}\text{NbS}_2$  crystal. The resulting susceptibility curve displayed a peak at 29K, which is consistent with previous studies (7, 8). Additionally, the downturn in the susceptibility indicates the emergence of antiferromagnetic order in the Co ions below the transition temperature. Figure S1F shows the results of the susceptibility measurement for both the magnetic field aligned with the  $c$ -axis and perpendicular to the  $c$ -axis.

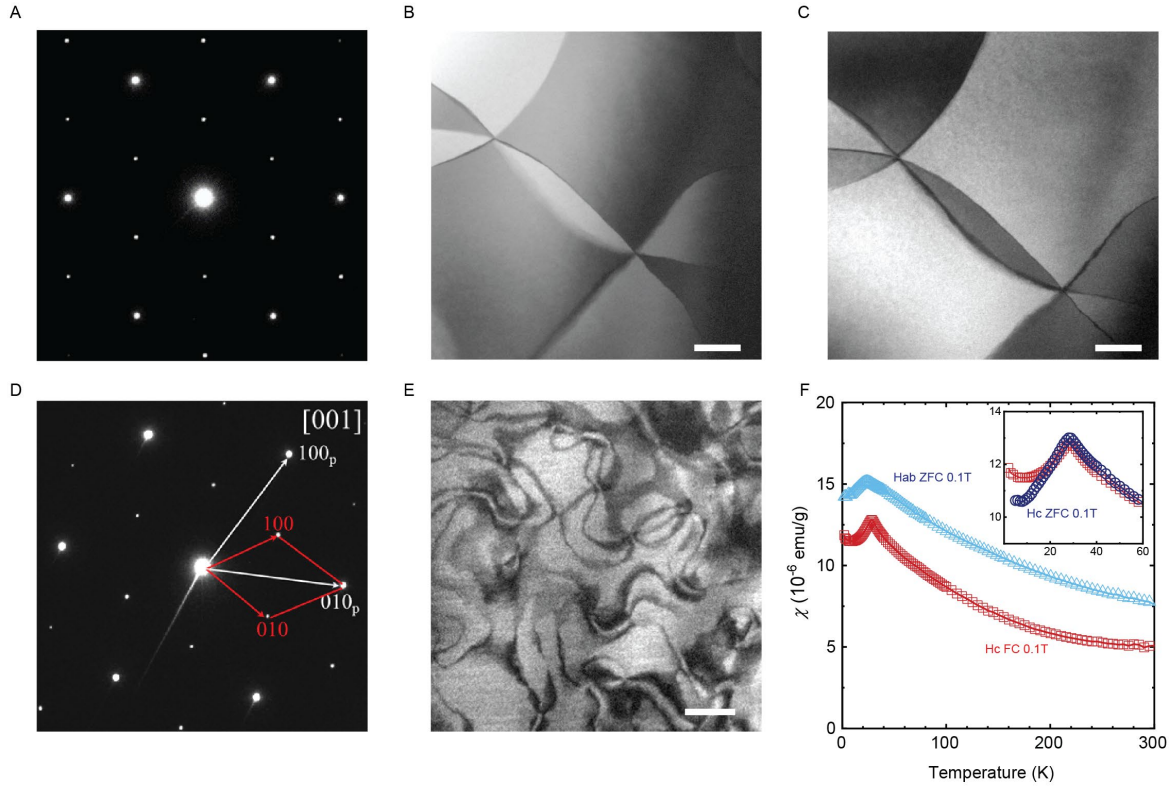


**Fig. S3. Manipulation of Topological Vortex Density with Cooling Rate.** (A) Selected area electron diffraction pattern along [001] direction remains intact after quenching, which means that the chiral structure does not change during quenching. (B,C) Contrast reversal of chiral domains with selective diffraction peak showing asymmetry in the Friedel pair. (D) The primitive cell and the tripled supercell diffraction peaks are depicted with the white and the red arrows, respectively. (E) Superlattice DF-TEM image of the quenched crystal showing a high density of topological defects with the size of a few hundred nanometers in contrast to the furnace cooled sample in Fig. 1B. The structural transition from primitive  $P6_3/mmc$  to chiral  $P6_322$  is estimated to be around  $1000^\circ\text{C}$  and the defect (vortex/antivortex) density has been changing according to the universal Kibble-Zurek mechanism, which shows the emergent continuous symmetry that describes the scaling of defect density at a finite cooling speed. (scale bar: 200 nm) (F) Temperature dependence of the magnetic susceptibility revealing the antiferromagnetic phase transition at 26 K. Several measurement schemes upon field cool/zero-field cool (FC/ZFC) or field along  $c$ -axis/ $ab$ -plane ( $H_c/H_{ab}$ ) are shown.

### Supplementary Note 3.

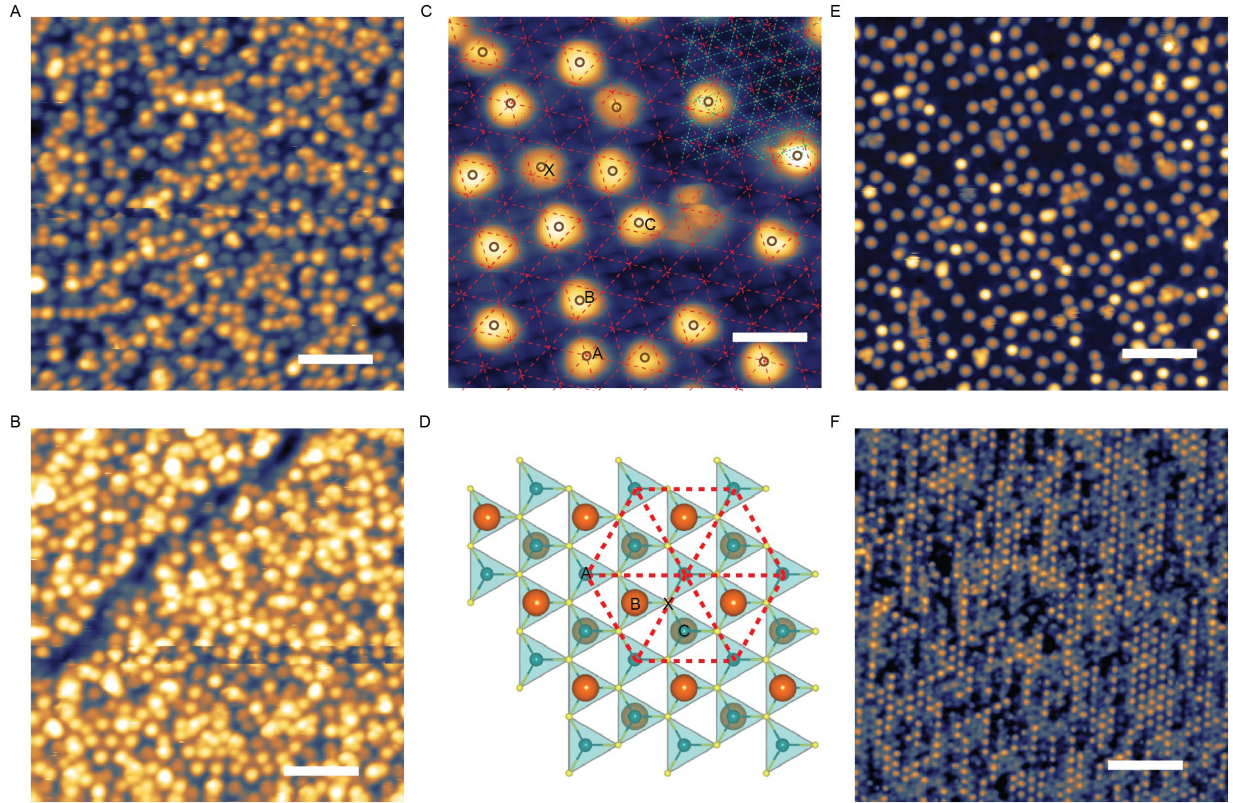
#### Effect of Cleaving Temperature on Cleaving Behavior

One of the defining characteristics of van der Waals materials is their ability to be cleaved, which results from the weak interlayer coupling in these materials. Similarly,  $\text{Co}_{1/3}\text{NbS}_2$  exhibits good cleavability, although the Co-intercalated structure requires a slightly stronger force to cleave compared to its parent material,  $\text{NbS}_2$ . Moreover, the cleaved Co-type surface exhibits different stability characteristics compared to other layered materials, with the exposed Co ions being less stable.

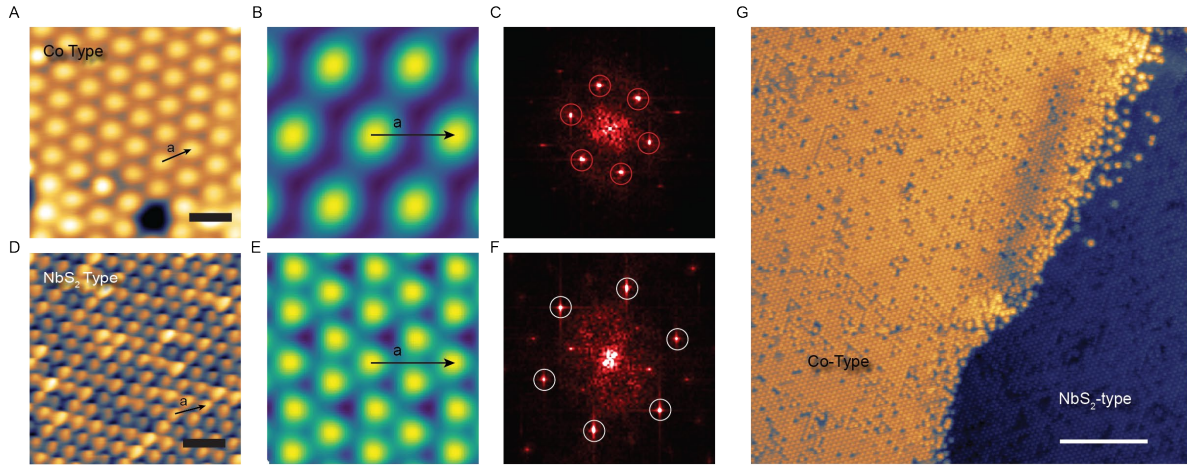
The Co ions in the van der Waals gap exhibit localized d-orbitals with a valence of 2+, resulting from charge transfer with the  $\text{NbS}_2$  matrix. This results in the formation of localized magnetic moments in the Co ions, which leads to the emergence of antiferromagnetic order at low temperatures. The stability of the isolated orbitals allows for the maintenance of the ordering at room temperature and no degradation within the bulk structure, as demonstrated by our DF-TEM measurements comparing crystals with different cooling rates (Fig. S3). The Co intercalants do not lose their ordering until they reach a temperature close to 1000°C, at which point they transform into a disordered high-temperature phase ( $\text{P6}_3/\text{mmc}$ ). However, this stability does not apply to Co ions on the surface. In our initial efforts to observe room temperature cleaved surfaces using STM, we found that the surfaces were highly disordered.

Fig. S4A shows an STM topography of a  $\text{Co}_{1/3}\text{NbS}_2$  surface that was cleaved at room temperature. Despite being transferred to the cryogenic measurement setup immediately after cleaving, meaning that the surface was exposed to room temperature for less than a few minutes, the surface appears completely disordered and no trace of the original  $(\sqrt{3} \times \sqrt{3})R30^\circ$  ordering of the Co lattice can be observed. However, we did observe interesting features showing Co-deficient linear feature, such as the one shown in Fig. S4B, which we believe that they are structural chiral domain boundaries.

The surface thermal diffusion of exposed intercalated ions at room temperature seems to be a common feature of isostructural 1/3 intercalated transition metal dichalcogenides (TMDs). Similar characteristics has been observed from  $\text{Co}_{1/3}\text{TaS}_2$  as well as  $\text{Ni}_{1/3}\text{TaS}_2$ , which we successfully synthesized together with  $\text{Co}_{1/3}\text{NbS}_2$  and conducted TEM and STM measurements. Figs. S4C and E show the topography of a  $\text{Co}_{1/3}\text{TaS}_2$  surface after cleaving at room temperature, and they also show similar diffusion of surface Co ions. The diffused movement is evident when it is compared with the ideal triangular arrangement of Co ions in Fig. S4D. To prevent the diffusion at room temperature, we have cleaved the samples at low temperature with cryogenic cooling using liquid nitrogen. The samples stay cooled at the stage for an hour with the temperature reading of about 80 K prior to cleaving. The low temperature cleaving results are markedly different as shown in the main text (Fig. 2 for  $\text{Co}_{1/3}\text{NbS}_2$ ) as well as in Fig. S4F for  $\text{Co}_{1/3}\text{TaS}_2$ . The low temperature cleaved surfaces show clear ordering of Co ions revealing  $(\sqrt{3} \times \sqrt{3})R30^\circ$ . In the case of  $\text{Co}_{1/3}\text{TaS}_2$  it can be seen that the number of Co left on the surface is less than that of  $\text{Co}_{1/3}\text{NbS}_2$ . That may be a result of different inter-layer coupling between  $\text{NbS}_2$  and  $\text{TaS}_2$ , or difference in Co concentration, and it will be subject to future investigation.



**Fig. S4. Temperature Dependent Cleaving Behavior.** (A) STM topography of a  $\text{Co}_{1/3}\text{NbS}_2$  surface cleaved at room temperature. (B) Another region showing a suspicious domain boundary-like feature. (-0.2 V, 50 pA, scale bar: 4 nm) (C) Atomic scale STM topography of room temperature cleaved  $\text{Co}_{1/3}\text{TaS}_2$ . The host material unit cell grid is shown as the dashed green mesh on the upper right corner, and the  $(\sqrt{3} \times \sqrt{3})R30^\circ$  unit cell grid is shown as the dashed red grid. The positions of surface Co ions are marked with black circles that can be compared with the crystallographic positions in the model of (D). While most of the positions are B, there exist also A, C, and X. (D) Registration of surface Co ions in the atomic model showing an AB-stacked structure. A, B, and C are as discussed in the main text, and X is the hollow site which is normally prohibited in the bulk structure. (E,F) Comparison of room temperature (E) and low temperature (F) cleaved surface of  $\text{Co}_{1/3}\text{TaS}_2$ . The low temperature cleaved one is showing the  $(\sqrt{3} \times \sqrt{3})R30^\circ$  ordering together with partial removal of surface Co ions during cleaving. (parameters of e: -50 mV, 100 pA, f: -20 mV, 500 pA, scale bars: 4 nm)



**Fig. S5. Co and NbS<sub>2</sub> Type Surfaces.** (A,B,C) STM topography, STM simulation image, and Fourier transformation of the topography from Co exposed type surface. (D,E,F) STM topography, STM simulation image, and Fourier transformation of the topography from NbS<sub>2</sub> exposed type surface. (scale bars in A, B = 0.7nm) The size of the lattice constant  $a$  are compared in the real space images and the simulations. The red circles are  $(\sqrt{3} \times \sqrt{3})R30^\circ$  superstructure peaks which correspond to reciprocal vectors of the lattice constant  $a$ . The white circles indicate the pristine  $(1 \times 1)$  peaks of NbS<sub>2</sub> structure. (G) a boundary of two different types of surfaces. (tunneling parameters are -0.02V, 30pA, scale bar = 10nm)

## Supplementary Note 4.

### Experimental Estimation of the Spin Polarization.

There are various types of magnetized tips that can be used in SP-STM, including ferromagnetic bulk, ferromagnetic coated, antiferromagnetic bulk, and antiferromagnetic coated tips, depending on the purpose of the measurement (9).  $\text{Co}_{1/3}\text{NbS}_2$  and its isostructural chiral intercalated TMDs display a range of magnetic orders that exhibit complex phase transitions as a function of temperature or magnetic field. In this study, we sought to minimize the effect of any intrinsic magnetic order, so it was necessary to minimize the stray magnetic field from the tip as it could affect the surface magnetic ordering of Co. It has been reported that the stray field from a ferromagnetic tip can reach up to 300 mT (10), which is typically not a problem for materials with large coercivity. However, the chiral 1/3 intercalated TMDs often exhibit magnetic orders (or anomalies) with very low critical fields. For example, the critical field for magnetoresistance in  $\text{Cr}_{1/3}\text{NbS}_2$  was reported to be around 170 mT (11). Therefore, the stray field from a ferromagnetic tip is sufficient to affect the magnetic ordering of 1/3 intercalated TMDs. Given these considerations, we believe that the use of an antiferromagnetic tip is essential for this study. We employed a material transfer method to coat the tip, which can be applied to a Cr(001) surface (12, 13). Pt/Ir alloy tip was prepared by bombarding it with an electron beam to remove any potential contamination, and then it was indented a few nanometers towards the Cr(001) surface while applying a few volts of negative bias to the tip. The tip was then pulled out at a speed of a few nm/s until the current dropped, and several repetitions of this process resulted in the successful transfer of Cr to the tip end.

To verify the magnetization of the Cr coated Pt/Ir tip, we used the layer-by-layer antiferromagnetic contrast of Cr(001) in tunneling spectroscopy. The Cr(001) surface shows a different magnetic ordering from the bulk due to the suppressed spin density wave and the absence of spin flip transition (14–16). It shows a magnetic structure, in which Cr magnetic moments ferromagnetically align within a layer and antiferromagnetically align between adjacent layers. As a result, the magnetization shows the rotation of  $\pi$  whenever it undergoes a single atom height step. We obtained the characteristic layer-by-layer contrast after repeated indentation. A representative result is shown in Figure S4, where a monoatomic step is shown alongside some traces of bulk impurities and particulate debris, which were created during the indentation process. The antiferromagnetic alignment of magnetic moment in the adjacent layers can be seen in the spatial-resolved tunneling spectroscopy in Fig. S6B. The drastic change of tunneling spectral intensity is shown by a contrast change across the step edge. The tunneling spectra obtained on the upper and the lower terrace are depicted in red and blue curves in Fig. S6C, respectively. The verified tips have showed a successful observation of spin contrast, as presented in the main text.

Typically, “asymmetry of differential conductance” spectra can be used to determine the spin-polarization of the tip, and eventually, that of the sample (17). However, we find that this is not possible here because Cr tips are known to show a randomly oriented magnetization (18), and we rely on the out-of-plane magnetization. The asymmetry within the plane of the Cr(001) surface could be obtained from the contrast associated with in-plane magnetization, but this does not provide the asymmetry perpendicular to the surface. Instead, we estimate the empirical spin polarization  $P$  using the formula,  $P = (I_{\uparrow\uparrow} - I_{\uparrow\downarrow}) / (I_{\uparrow\uparrow} + I_{\uparrow\downarrow})$ , where  $I_{\uparrow\uparrow} = I_0(1 + P)$  and  $I_{\uparrow\downarrow} = I_0(1 - P)$ . Utilizing the observed height difference and the work function, we can estimate  $P$  based on an exponential dependence of tunneling current to the tip height following (19, 20) as

$$P(\Delta z) = \frac{\exp\left(A\sqrt{\tilde{\phi}}\Delta z\right) - 1}{\exp\left(A\sqrt{\tilde{\phi}}\Delta z\right) + 1}$$

where  $A \approx 1eV^{-1/2}\text{\AA}^{-1}$  and  $\tilde{\phi}$  is the mean local tunneling barrier height. Under the assumption that  $\tilde{\phi} \approx (\phi_{sample} + \phi_{Cr})/2 \approx \phi_{Cr}$ , the measured  $\Delta z \approx 0.22 \text{\AA}$  and  $\phi_{Cr} = 4.5eV$  (21) give a value of  $P \approx 0.22$ . This value is comparable to the asymmetry in the tunneling spectra shown in the inset of Fig. 4E, where a 10% difference corresponds to  $P \approx 0.2$ . The presented estimates, however, are subject to several limitations. One arises from the uncertain orientation of tip magnetization, as discussed earlier. Additionally, the involvement of the orbital moment and its intricate interplay with spin polarization, as recently elucidated (22), remains a subject of further exploration.

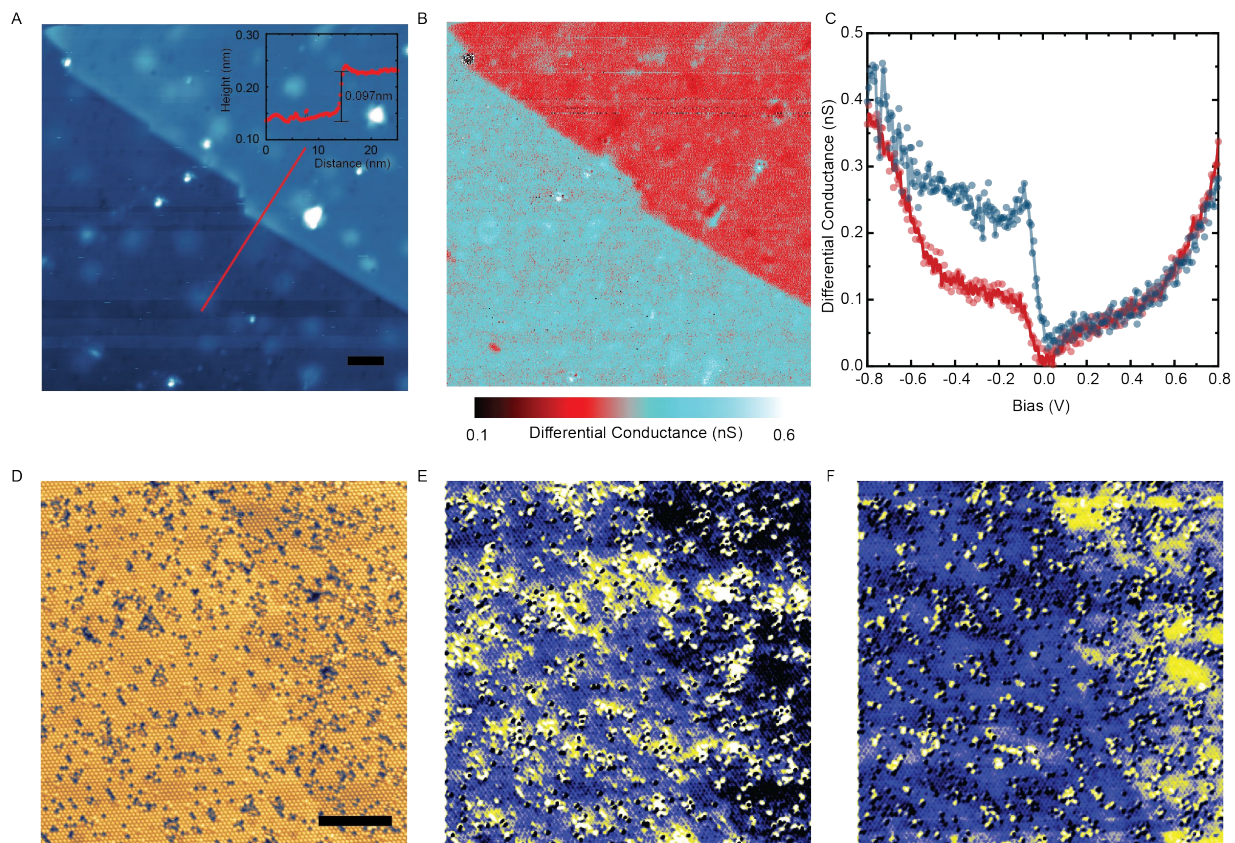


**Fig. S6. Verification of Magnetized Tip and Contrast Reversal.** (A) STM topography of Cr(001) surface with a monatomic step edge. (-0.3 V, 100 pA, scale bar: 5 nm) The height profile, illustrated in the inset along the red line, unveils a monatomic step measuring 0.097 nm. This value is diminished from the actual 0.14 nm due to the magnetic contribution, which usually produces alternating variation of step heights (16). (B) Spatial-resolved spin-polarized tunneling spectroscopy of the same region measured at -0.3 V. Clear contrast change due to the antiferromagnetic alignment of adjacent Cr layers is shown. (C) spin-polarized tunneling spectra obtained from the upper (red) and lower (blue) terrace in (A). The parallel (blue) and antiparallel (red) alignment of the tip magnetization and the surface magnetic moment produces two different tunneling spectra. (D) STM topography of a region with a structural chiral domain boundary (-5mV, 10pA, scale bar: 10nm) (E) Spatial map of dI/dV taken from the same area of (D) at -50mV. The tip height is recorded at a tunneling condition of -5mV, 10pA during topography scan and the path is replayed to take dI/dV at -50mV. (F) dI/dV from the same area at +50mV. The tip height is recorded at a tunneling condition of +5mV, 10pA during topography scan and the path is replayed to take dI/dV at +50mV.

## Supplementary Note 5.

### Atomic Model of Chiral Domain Boundaries around a Topological Vortex

Research on chiral  $1/3$  intercalated TMDs has been ongoing for several decades due to the various magnetisms that can be tuned by the intercalant species and the host matrix material (23). In particular, the  $\text{Cr}_{1/3}\text{NbS}_2$  variant exhibits in-plane ferromagnetic order and has been observed to display helical magnetic order as a result of the competition between the ferromagnetic coupling, which prefers parallel alignment, and the interlayer Dzyaloshinskii-Moriya interaction, which prefers perpendicular alignment (11). In addition to this, the large anomalous Hall effect of  $\text{Co}_{1/3}\text{NbS}_2$  has garnered significant attention due to the accompanying magnetization anomaly near the antiferromagnetic phase transition (24).

A common feature of all chiral  $1/3$  intercalated TMDs is the formation of six domains surrounding a topological vortex due to domain boundaries resulting from structural chirality and antiphase. However, little research has been conducted on the interaction of the aforementioned exotic magnetic states with topological vortices and chiral domains in real space. In particular, it is revealed that the handedness of the magnetic helicity in the case of helical magnetic order is determined by structural chirality (25). However, there has been no exact atomic model of domain boundaries to date, which presents a challenge (5). Therefore, providing a precise atomic model of the topological vortex and chiral domains would be beneficial for further understanding of the interaction between structural chirality and helical magnetism. Based on STM observations, we present an atomic-scale model of structural chiral domains around a topological vortex. To the best of our knowledge, there has been no spatially resolved surface study on chiral domains/boundaries at the atomic-scale and topological vortex networks in any of the  $1/3$  intercalated TMDs. It is likely that this model can be applied to most isostructural  $1/3$  intercalated TMDs.

Fig. S7A is the atomic model of a chiral structural domain boundary drawn in accordance with the observation in Fig. 2A. The model assumes an idealized straight domain boundary, although real ones tend to have a curved orientation change. However, this does not alter the fact that the domain boundary has a lower density of Co ions compared to the inside region of a domain. This Co-deficient nature is represented in the schematic by the inter-row distance between the normal and boundary regions. The model illustrates the shift in the Co lattice on the surface (solid blue to solid red circles), while the lattice underneath remains unchanged (hollow green circles). A similar model can be constructed for the second type by exchanging the surface Co and the underneath Co lattice. It should be noted that the model previously proposed (5) by the author and the model presented at this time are different in that the intercalant density is lower near the domain boundary, but the change does not give a difference to the extinction rule observed in the DF-TEM result (5). Whether the boundary region gives additional or deficient number of Co intercalant does not change the fact that the region has antiphase shift along all three equivalent  $\mathbf{q}$  directions, and it makes the boundary observable in DF-TEM relevant to all three  $(\sqrt{3} \times \sqrt{3})R30^\circ$  superlattice peak directions. Nevertheless, that can be of importance when one tries to study the interaction of the localized magnetic moments of Co ions across a domain boundary.

Six chiral structural domain boundaries converge at a topological vortex, which exhibits a topological robustness. The robustness means that a topological vortex cannot be removed by themselves, and can be removed only by going out of the sample or annihilated by the recombination with a nearby antivortex. The topological robustness can be witnessed in the

structure of the domain boundary. Fig. S7B shows the approach and the (virtual) crossing of two chiral structural domain boundaries. The two domain boundaries change the intercalant site across the crossing point. (i.e. the solid line exchanges the solid blue and red circles. The dashed line changes the hollow red and green circles.) However, their crossing at the center resulted in a switch of both of the Co lattice and eventually forms a AA-type stacking. As the crystal structure only allows AB-type stacking, we can see that the crossing of two different type domain boundaries is not allowed. As a result, the vortex structure shown in Fig. S7C forms a topologically robust defect while the order of domain appearance cannot be altered.

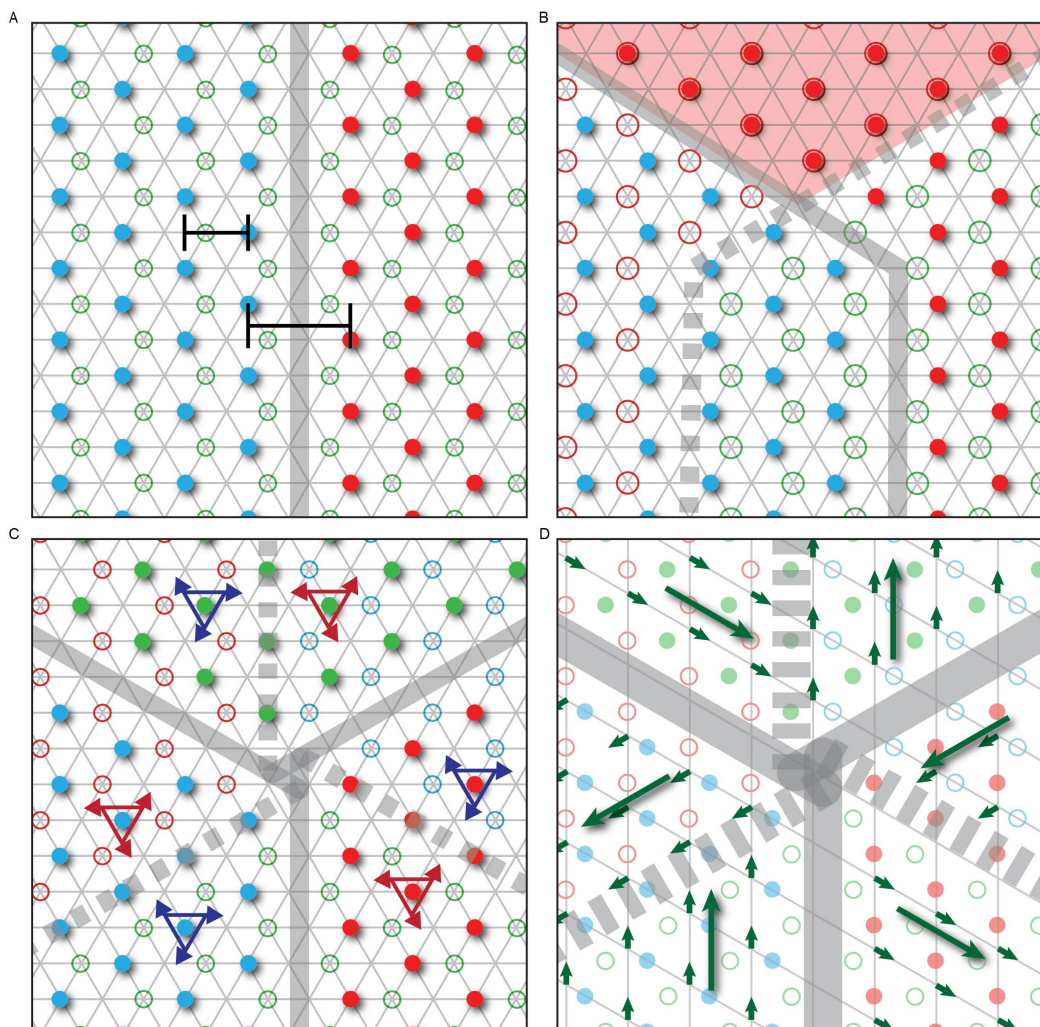


**Fig. S7. Atomic Model of Chiral Structural Domain Boundary and Topological Vortex.** **(A)** Atomic model of Upper domain boundary. The Co intercalation site is changed in Upper Co lattice from blue to red circles across the boundary, while that of Lower Co lattice (green circle) is intact. The Co deficient nature of the boundary is represented by the average distance between Co rows inside the domain and the domain boundary region. **(B)** Prohibition of domain-boundary crossing. Crossing of the Upper (solid line) and the Lower (dashed line) domain boundary results in a formation of the AA-type stacking (red shade) that is prohibited in the crystal structure. The mechanism forces the domains not to change the order of appearance around a topological vortex and contribute to the topological robustness of the vortex structure. **(C)** Atomic model of a topological vortex and nearby chiral structural domains. The alternating arrangement of Upper and Lower domain boundaries results in a complete circulation through all the permutations of the stacking sequence. The opposite chiralities are depicted by the red and the blue triangular arrows. **(D)** The atomic model of a topological vortex is analyzed by examining the change in displacement vectors in relation to a unit cell grid. The hexagonal unit cell grid is overlaid on all six domains and the displacement vectors of the sulfur ions (located at the crossing points) are analyzed. These vectors rotate by  $2\pi/3$  across a boundary and result in a complete  $4\pi$  rotation around the vortex. It is important to note that two domains with the same displacement vector direction exhibit opposite stacking sequences, which prevents the dissociation of the vortex.

## Supplementary Note 6.

### Rotation of Displacement Vector around a Topological Vortex

The topological robustness the vortex can be examined in the change of the displacement vectors of the sulfur lattice where we can define topological charge (3, 26). Fig. S7D shows the change of the sulfur displacement vectors that is projected onto the unit cell grid, meaning they are analyzed by the modulus of the unit cell translation. The shift of the Upper or the Lower Co at the domain boundary causes the displacement vectors to rotate by  $2\pi/3$  between any adjacent domains. When the displacement vector completes a winding around the vortex, it has undergone a  $4\pi$  rotation. It is important to note that in the case of two opposite domains with the same sulfur displacement vector, they have reversed stacking sequences due to the anti-phase shift. The completion of a  $4\pi$  rotation represents a completed circular pattern in the discrete order parameter space formed using the S displacement vector as an order parameter (27). To remove this circular pattern, one must pass through the center point, which requires breaking the chiral distortion of the crystal structure. Similar entangled domain boundaries and their robustness can be found in various systems (3) such as hybrid improper ferroelectrics (28), incommensuration in charge density wave (26), or dislocation in metal interfaces (29).

## Supplementary Note 7.

### Determination of the Zero Crossing Point

When we obtain tunneling spectra from domains with opposite chiralities, it is immediately discernable to find the different slopes in differential conductance. Since it is only observed with magnetic probe, the different slopes indicate that the spin-polarized signal contributes in opposite ways in domains with different chiralities. However, determining the exact crossing point, where the current-induced magnetization vanishes, is a sophisticated problem. In general, tunneling spectra of STM are measured using a constant tip height to eliminate any changes in the tunneling barrier between the tip and the sample. However, the selection of the tip height, which is determined by the combination of applied bias and tunneling current, is subject to various experimental factors. The normalization bias, which is the applied bias before the feedback is open, is usually chosen to be far from features of interest in the spectrum. In this case, we had to select the normalization bias close to the point where the spectra have vanished current-induced magnetization (i.e., near the zero bias). This was done by tracing the systematic change in the spectra with reducing normalization biases. In other words, the crossing point was measured with various normalization biases, and we found that the crossing point converged towards zero bias as the normalization bias moved towards zero.

Fig. S8 shows schematics illustrating the effect of tip height variation with positive (Fig. S8C) and negative (Fig. S8B) normalization biases. The crossing point, initially located at zero bias (Fig. S8A), shifts to positive or negative energy according to the normalization bias change. Fig. S8D shows the two representative spectra showing the effect of the normalization bias change. The solid and hollow curves show spectra using normalization biases of -10 mV and +10 mV, respectively. The crossing points were measured at -9.5 mV and +6.5 mV, respectively, which are both located between the normalization bias and zero. By bringing the normalization bias closer to zero, the crossing point converges to zero regardless of the chosen bias polarity. As a result of this convergence, we were able to determine that the effect of MTE vanishes at zero bias. Since the normalization bias cannot be located exactly at zero bias due to the instability of the feedback system, the spectra shown in the main text were obtained by averaging two measurements with normalization biases of +1 mV and -1 mV.

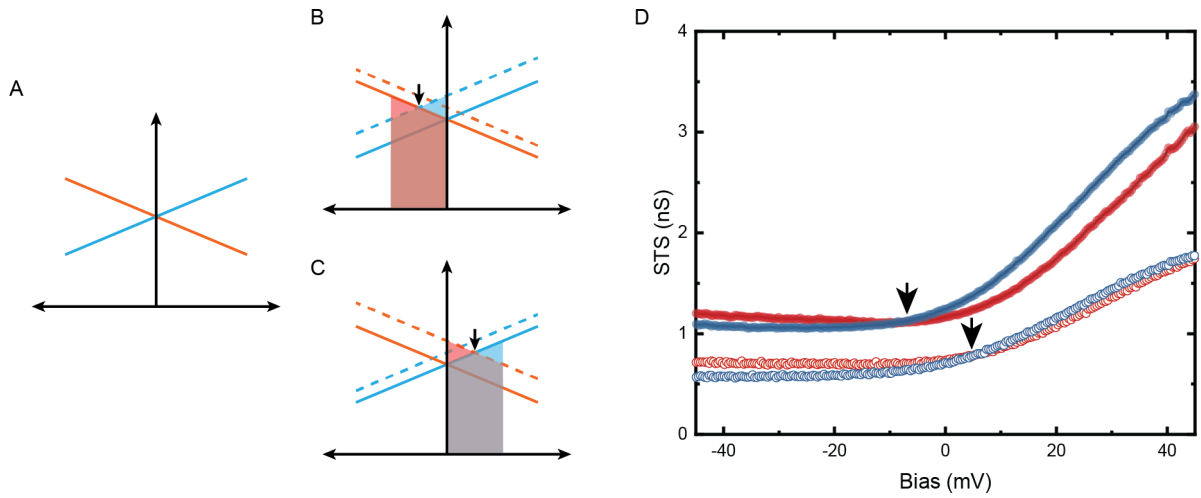


**Fig. S8. Determination of the Crossing Point.** (A) The ideal spectra with different slopes showing BCD induced magnetization in different chiral domains. (B,C) Schematics showing the change of crossing point when a negative (B) or positive (C) normalization bias is used. (D) Two sets of spin-polarized tunneling spectra obtained with the normalization biases of -10 mV (solid) and +10 mV (hollow). The red and blue colors depict two domains with opposite chiralities. The crossing points for the two biases were measured at -9.5 mV and +6.5 mV, respectively. (black arrows) There observed a systematic convergence of the crossing points towards zero bias as the normalization bias approaches to zero in both bias polarities.

## Supplementary Note 8.

### Crystal Structures used in DFT Calculations

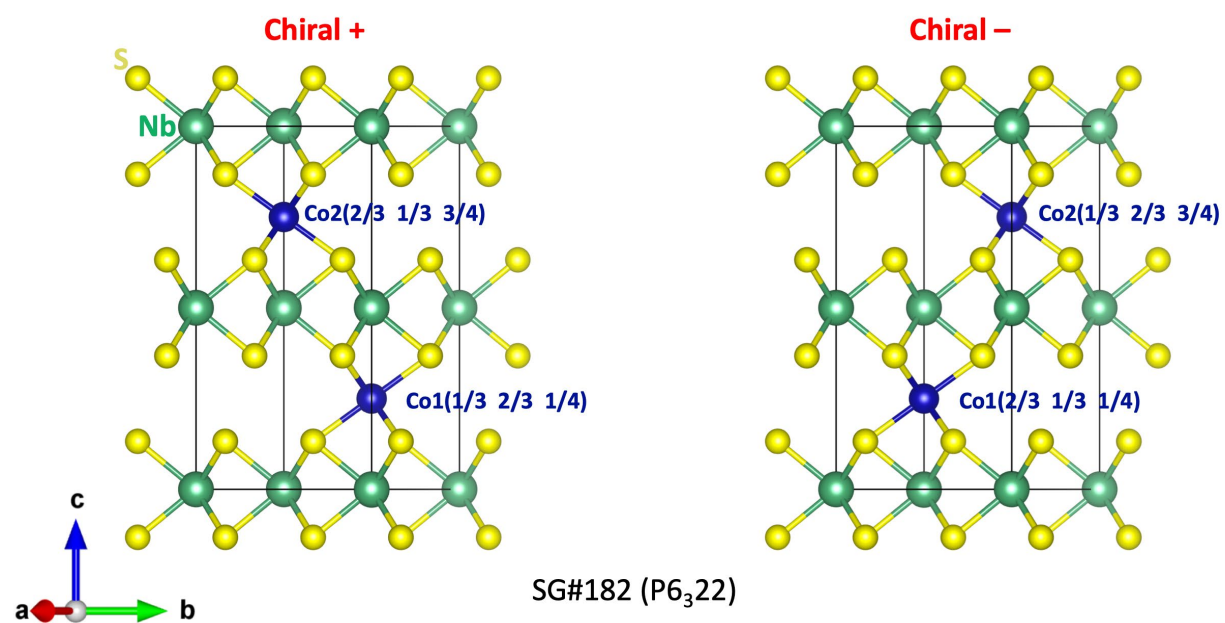


Fig. S9. Both inverted chiral structures of  $\text{Co}_{1/3}\text{NbS}_2$  in space group #182 ( $P6_322$ ).

## Supplementary Note 9.

### Role of Different Magnetic Configurations

We investigated the influence of different magnetic orderings on the two Co sites within a unit cell. We included spin-orbit coupling (SOC) and chose the [001] direction as the easy axis. Our DFT+U+SOC calculations showed that ferromagnetic (FM) ordering along the [001] direction had the lowest energy compared to antiferromagnetic (AFM) ordering, while the nonmagnetic configuration had the highest energy compared to both FM and AFM orderings. This held true for all values of the Hubbard  $U$  parameter we considered. Additionally, we estimated the magnetic exchange parameter ( $J$ ) for  $U = 5$  eV and obtained  $JS^2 = -4.80$  meV, where  $S$  is the spin state of Co and the negative sign indicates a FM coupling along the  $c$ -axis between nearest-neighbor Co sites within the home unit cell. These results are consistent with a previous study (30).

Fig. S10 shows the electronic band structure of  $\text{Co}_{1/3}\text{NbS}_2$  calculated with inclusion of SOC ( $U = 5$  eV and  $J = 1$  eV) for the nonmagnetic, FM, and AFM configurations. All three magnetic configurations yield metallic ground states.

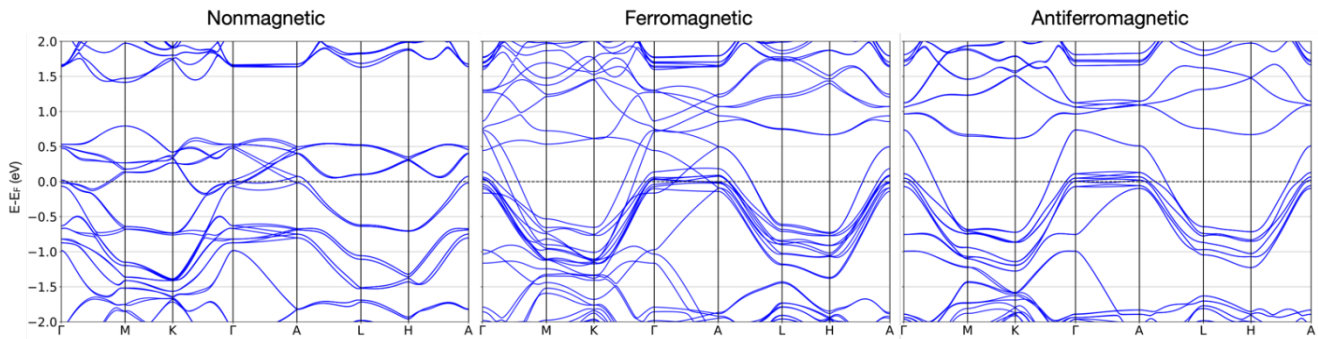


**Fig. S10.** Electronic band structure (with-SOC) calculated using  $U = 5$  eV and  $J = 1$  eV for three different magnetic orderings. The horizontal dashed line marks the Fermi level.

## Supplementary Note 10.

### Role of the Hubbard $U$ Parameter on the Electronic Band Structure

To examine the impact of the Hubbard  $U$  parameter on the electronic properties of nonmagnetic  $\text{Co}_{1/3}\text{NbS}_2$ , we varied the  $U$  parameter from 3 to 6 eV (with  $J$  set to 1 eV for all cases) and calculated the electronic band structure with the inclusion of spin-orbit coupling (SOC). Our results, shown in Fig. S11, indicate that there are no significant changes in the electronic properties within this range of  $U$  parameters, such as the opening of a bandgap at the Fermi level. This is as expected for the nonmagnetic case.

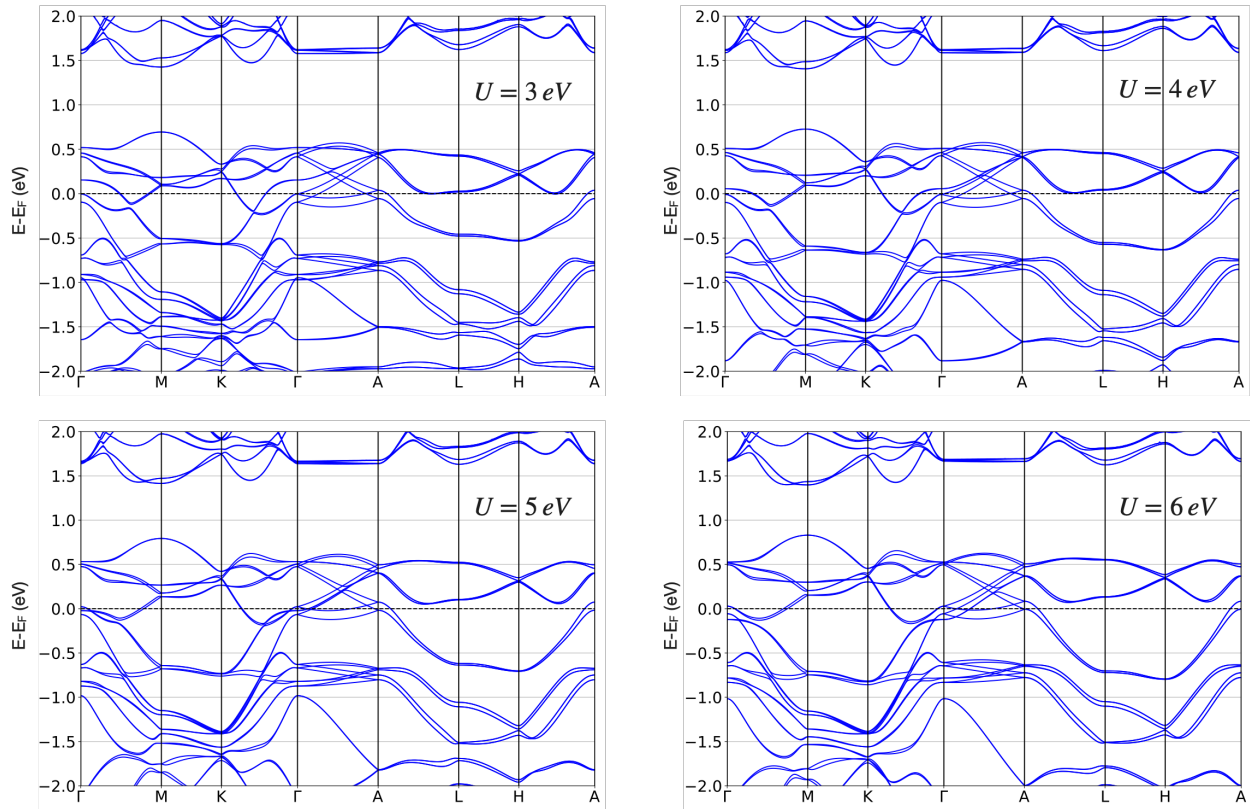


**Fig. S11.** DFT+U+SOC calculated electronic band structure for different values of Hubbard  $U$  parameter ( $J = 1$  eV) for nonmagnetic  $\text{Co}_{1/3}\text{NbS}_2$ . The horizontal dashed line marks the Fermi level.

## Supplementary Note 11.

### Qualitative Estimation of the $z$ Component of Magnetization ( $M_z$ )

In order to qualitatively estimate the  $z$  component of current-induced magnetization, we recall the relationship between the current-induced magnetization and BCD tensor,  $M_z \propto D_{zz} J_z$  (31–33), where  $D_{zz}$  is the  $zz$  component of BCD tensor and  $J_z$  is the current density along  $z$  axis.  $D_{zz}$  is calculated using the below equation as implemented in the WannierBerri package (34).

$$D_{zz}(E_F) = \int [d\mathbf{k}] \sum_n^{occ} [d\mathbf{k}] \frac{\partial E_{n,\mathbf{k}}}{\partial k_z} \Omega_n^z \delta(E_{n,\mathbf{k}} - E_F)$$

Here  $E_F$  denotes the Fermi energy,  $E_{n,\mathbf{k}}$  represents  $n^{\text{th}}$  energy eigenstate of Bloch electrons at crystal momentum  $\mathbf{k}$ , and  $\Omega_n^z$  represents the  $z$  component of Berry curvature of the  $n^{\text{th}}$  eigenstate in the momentum space. To qualitatively estimate the BCD-induced magnetization, we multiply the calculated  $D_{zz}$  (shown in Fig. S12A) with the cumulative density of states minus the total number of valence electrons  $N_e$  near the Fermi level (shown in Fig. S12B), which gives us a qualitative estimation of the electronic current density ( $J_z$ ) under a bias voltage. We found that the values of  $D_{zz}$  are quite large when compared to the reported BCD in previously studied bulk systems (35–38). Also, we note that  $D_{zz}$  reverses its sign upon the chirality reversal. The overall product of  $D_{zz}$  and  $J_z$  yields an estimation of current-induced  $M_z$  (in arbitrary units) for both chiral structures of nonmagnetic  $\text{Co}_{1/3}\text{NbS}_2$ , as shown in Fig. S12C. The calculation is in line with the strain induced valley magnetization although it derived considering some approximations for semiconducting  $\text{MoS}_2$  monolayer having a bandgap at the Fermi level (33). Nonetheless, the calculation of  $M_z$  using the relation,  $M_z \propto D_{zz} J_z$ , provides a good qualitative description. Especially, the antisymmetric behavior is consistent with the symmetry considerations as well as with the quantitative calculation in the framework of MTE as shown in Fig. 1B and 4C.

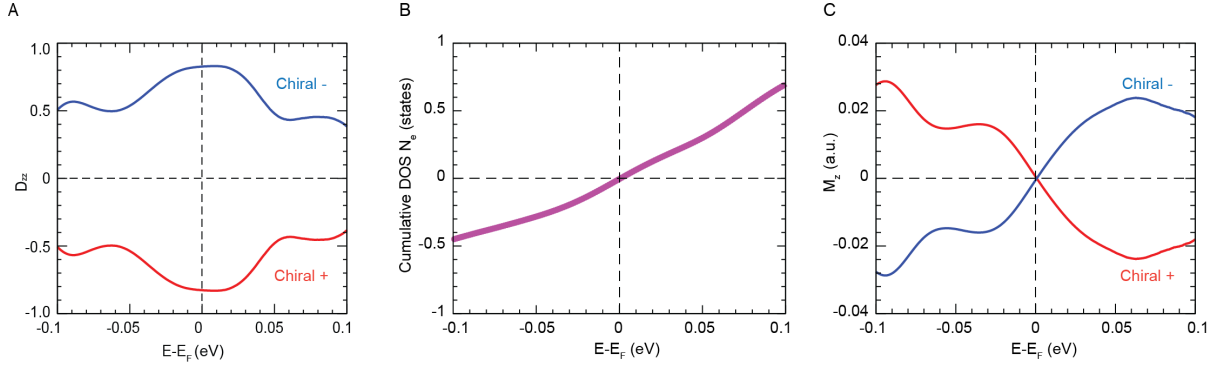


**Fig. S12.** (A) Calculated BCD component along  $z$  axis ( $D_{zz}$ ) based on the DFT+U+SOC calculation ( $U = 5$  eV,  $J = 1$  eV) as a function of energy near the Fermi level. (B) Cumulative density of states (DOS) minus the total number of valence electrons ( $N_e$ ) plotted as the chemical potential near the Fermi level for the nonmagnetic  $\text{Co}_{1/3}\text{NbS}_2$ . (C) Product of the cumulative DOS data reported in the left panel with  $D_{zz}$  which gives a qualitative estimate of current-induced  $M_z$  (in arbitrary units) for both the chiral structures of nonmagnetic  $\text{Co}_{1/3}\text{NbS}_2$ .

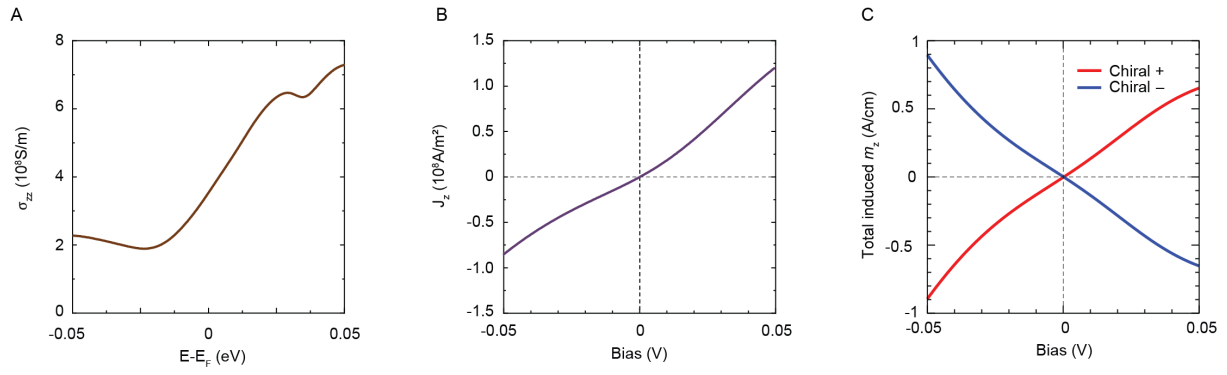


**Fig. S13. (A)** Ohmic conductivity  $\sigma_{zz}$  calculated from the DFT result as a function of chemical potential from the Fermi energy **(B)** Experimental current density measured in unit of  $\text{A/m}^2$  that is used to calculate the results in Fig. 4. The current data taken in Fig. 4I are averaged and divided by the typical size of tunneling area. **(C)** Total induced  $m_z$  shown in unit of  $\text{A/cm}$  using the experimental current density and  $K_{zz}$  before it is converted to  $\mu_B/\text{cell}$  units.

## References

1. S.-W. Cheong, S. Lim, K. Du, F.-T. Huang, Permutable SOS (symmetry operational similarity). *npj Quantum Mater.* **6**, 1–10 (2021).
2. S.-W. Cheong, SOS: symmetry-operational similarity. *npj Quantum Mater.* **4**, 1–9 (2019).
3. F.-T. Huang, S.-W. Cheong, Aperiodic topological order in the domain configurations of functional materials. *Nature Reviews Materials* **2**, 17004 (2017).
4. S.-W. Cheong, F.-T. Huang, M. Kim, Linking emergent phenomena and broken symmetries through one-dimensional objects and their dot/cross products. *Rep. Prog. Phys.* **85**, 124501 (2022).
5. Y. Horibe, *et al.*, Color Theorems, Chiral Domain Topology, and Magnetic Properties of Fe<sub>x</sub>TaS<sub>2</sub>. *J. Am. Chem. Soc.* **136**, 8368–8373 (2014).
6. S.-Z. Lin, *et al.*, Topological defects as relics of emergent continuous symmetry and Higgs condensation of disorder in ferroelectrics. *Nature Phys* **10**, 970–977 (2014).
7. G. Tenasini, *et al.*, Giant anomalous Hall effect in quasi-two-dimensional layered antiferromagnet Co<sub>1/3</sub>NbS<sub>2</sub>. *Phys. Rev. Research* **2**, 023051 (2020).
8. S. S. P. Parkin, E. A. Marseglia, P. J. Brown, Magnetic structure of Co<sub>1/3</sub>NbS<sub>2</sub> and Co<sub>1/3</sub>TaS<sub>2</sub>. *J. Phys. C: Solid State Phys.* **16**, 2765 (1983).
9. R. Wiesendanger, Spin mapping at the nanoscale and atomic scale. *Rev. Mod. Phys.* **81**, 1495–1550 (2009).
10. A. Kubetzka, M. Bode, O. Pietzsch, R. Wiesendanger, Spin-Polarized Scanning Tunneling Microscopy with Antiferromagnetic Probe Tips. *Phys. Rev. Lett.* **88**, 057201 (2002).
11. L. Wang, *et al.*, Controlling the Topological Sector of Magnetic Solitons in Exfoliated Cr<sub>1/3</sub>NbS<sub>2</sub> Crystals. *Phys. Rev. Lett.* **118**, 257203 (2017).
12. S. Choi, *et al.*, Switching Magnetism and Superconductivity with Spin-Polarized Current in Iron-Based Superconductor. *Phys. Rev. Lett.* **119**, 227001 (2017).
13. W. Ko, E. F. Dumitrescu, P. Maksymovych, Statistical detection of Josephson, Andreev, and single quasiparticle currents in scanning tunneling microscopy. *Phys. Rev. Research* **3**, 033248 (2021).
14. T. Hänke, *et al.*, Absence of spin-flip transition at the Cr(001) surface: A combined spin-polarized scanning tunneling microscopy and neutron scattering study. *Phys. Rev. B* **71**, 184407 (2005).
15. M. Kleiber, M. Bode, R. Ravlić, N. Tezuka, R. Wiesendanger, Magnetic properties of the Cr(001) surface studied by spin-polarized scanning tunneling spectroscopy. *Journal of Magnetism and Magnetic Materials* **240**, 64–69 (2002).
16. M. Kleiber, M. Bode, R. Ravlić, R. Wiesendanger, Topology-Induced Spin Frustrations at the Cr(001) Surface Studied by Spin-Polarized Scanning Tunneling Spectroscopy. *Phys. Rev. Lett.* **85**, 4606–4609 (2000).
17. F. Donati, *et al.*, Electronic and magnetic properties of bulk Cr tips for scanning tunneling spectroscopy. *Phys. Rev. B* **87**, 235431 (2013).
18. A. Schlenhoff, S. Krause, G. Herzog, R. Wiesendanger, Bulk Cr tips with full spatial magnetic sensitivity for spin-polarized scanning tunneling microscopy. *Appl. Phys. Lett.* **97**, 083104 (2010).
19. M. Enayat, *et al.*, Real-space imaging of the atomic-scale magnetic structure of Fe<sub>1+y</sub>Te. *Science* **345**, 653–656 (2014).

20. R. Wiesendanger, H.-J. Güntherodt, G. Güntherodt, R. J. Gambino, R. Ruf, Observation of vacuum tunneling of spin-polarized electrons with the scanning tunneling microscope. *Phys. Rev. Lett.* **65**, 247–250 (1990).
21. T. J. Drummond, Work Functions of the transition Metals and Metal Silicides. *Journal of Applied Physics* (1999) (November 27, 2023).
22. Y. Xing, *et al.*, Localized spin-orbit polaron in magnetic Weyl semimetal Co<sub>3</sub>Sn<sub>2</sub>S<sub>2</sub>. *Nat Commun* **11**, 5613 (2020).
23. S. S. Parkin, R. H. Friend, 3d transition-metal intercalates of the niobium and tantalum dichalcogenides i. Magnetic properties. *Philosophical Magazine B: Physics of Condensed Matter; Statistical Mechanics, Electronic, Optical and Magnetic Properties* **41**, 65–93 (1980).
24. N. J. Ghimire, *et al.*, Large anomalous Hall effect in the chiral-lattice antiferromagnet CoNb<sub>3</sub>S<sub>6</sub>. *Nature Communications* **9**, 3280 (2018).
25. K. Du, *et al.*, Topological spin/structure couplings in layered chiral magnet Cr<sub>1/3</sub>TaS<sub>2</sub>: The discovery of spiral magnetic superstructure. *PNAS* **118** (2021).
26. S. Lim, J. Kim, C. Won, S.-W. Cheong, Atomic-Scale Observation of Topological Vortices in the Incommensurate Charge Density Wave of 2H-TaSe<sub>2</sub>. *Nano Lett.* **20**, 4801–4808 (2020).
27. N. D. Mermin, The topological theory of defects in ordered media. *Rev. Mod. Phys.* **51**, 591–648 (1979).
28. Y. S. Oh, X. Luo, F.-T. Huang, Y. Wang, S.-W. Cheong, Experimental demonstration of hybrid improper ferroelectricity and the presence of abundant charged walls in (Ca,Sr)<sub>3</sub>Ti<sub>2</sub>O<sub>7</sub> crystals. *Nat Mater* **14**, 407–413 (2015).
29. S. Shao, J. Wang, A. Misra, R. G. Hoagland, Spiral Patterns of Dislocations at Nodes in (111) Semi-coherent FCC Interfaces. *Scientific Reports* **3**, 1–7 (2013).
30. P. Popčević, *et al.*, Electronic transport and magnetism in the alternating stack of metallic and highly frustrated magnetic layers in Co<sub>1/3</sub>NbS<sub>2</sub>. *Phys. Rev. B* **107**, 235149 (2023).
31. T. Yoda, T. Yokoyama, S. Murakami, Current-induced Orbital and Spin Magnetizations in Crystals with Helical Structure. *Scientific Reports* **5**, 1–7 (2015).
32. T. Yoda, T. Yokoyama, S. Murakami, Orbital Edelstein Effect as a Condensed-Matter Analog of Solenoids. *Nano Lett.* **18**, 916–920 (2018).
33. J. Son, K.-H. Kim, Y. H. Ahn, H.-W. Lee, J. Lee, Strain Engineering of the Berry Curvature Dipole and Valley Magnetization in Monolayer MoS<sub>2</sub>. *Phys. Rev. Lett.* **123**, 036806 (2019).
34. S. S. Tsirkin, High performance Wannier interpolation of Berry curvature and related quantities with WannierBerri code. *npj Comput Mater* **7**, 1–9 (2021).
35. J. I. Facio, *et al.*, Strongly Enhanced Berry Dipole at Topological Phase Transitions in BiTeI. *Phys. Rev. Lett.* **121**, 246403 (2018).
36. Y. Zhang, Y. Sun, B. Yan, Berry curvature dipole in Weyl semimetal materials: An ab initio study. *Phys. Rev. B* **97**, 041101 (2018).
37. S. Singh, J. Kim, K. M. Rabe, D. Vanderbilt, Engineering Weyl Phases and Nonlinear Hall Effects in Td-MoTe<sub>2</sub>. *Phys. Rev. Lett.* **125**, 046402 (2020).
38. Z. Z. Du, H.-Z. Lu, X. C. Xie, Nonlinear Hall effects. *Nat Rev Phys* **3**, 744–752 (2021).

